## PHYSICAL SCIENCES

# Design of ultrathin Pt-Mo-Ni nanowire catalysts for ethanol electrooxidation

Junjie Mao,[1]* Wenxing Chen,[1]* Dongsheng He,[2]* Jiawei Wan,[1] Jiajing Pei,[1] Juncai Dong,[3] Yu Wang,[4] Pengfei An,[3] Zhao Jin,[5,6] Wei Xing,[5,6] Haolin Tang,[7] Zhongbin Zhuang,[8] Xin Liang,[9] Yu Huang,[1,10] Gang Zhou,[9] Leyu Wang,[9] Dingsheng Wang,[1†] Yadong Li[1†]

Developing cost-effective, active, and durable electrocatalysts is one of the most important issues for the commercialization of fuel cells. Ultrathin Pt-Mo-Ni nanowires (NWs) with a diameter of ~2.5 nm and lengths of up to several micrometers were synthesized via a $H_2$-assisted solution route (HASR). This catalyst was designed on the basis of the following three points: (i) ultrathin NWs with high numbers of surface atoms can increase the atomic efficiency of Pt and thus decrease the catalyst cost; (ii) the incorporation of Ni can isolate Pt atoms on the surface and produce surface defects, leading to high catalytic activity (the unique structure and superior activity were confirmed by spherical aberration–corrected electron microscopy measurements and ethanol oxidation tests, respectively); and (iii) the incorporation of Mo can stabilize both Ni and Pt atoms, leading to high catalytic stability, which was confirmed by experiments and density functional theory calculations. Furthermore, the developed HASR strategy can be extended to synthesize a series of Pt-Mo-M (M = Fe, Co, Mn, Ru, etc.) NWs. These multimetallic NWs would open up new opportunities for practical fuel cell applications.

## INTRODUCTION

In the past decades, considerable attention has been paid to high-performance fuel cells, which directly convert chemical energy into electrical energy with high efficiency and do not emit harmful gases. Among several kinds of fuel cells, direct ethanol fuel cells (DEFCs) have gained attention because of their high energy density, high conversion efficiency, light weight, and relatively low operating temperature (1). Nevertheless, the sluggish kinetics of anodic oxidation and vulnerable CO poisoning effect hamper its applications in the practical fuel cell and thus activate extensive research interests in this area.

Platinum (Pt) is one of the most commonly used electrocatalysts (2). To promote the eventual large-scale commercialization of fuel cells, efforts have been devoted to improving Pt-based materials to obtain cost-effective, active, and durable electrocatalysts (3–6). From the point of Pt atomic efficiency, one effective approach to decreasing the cost of electrocatalysts is to construct one-dimensional (1D) ultrathin nanowires (NWs) (with a typical diameter of less than 5 nm), which have inherent anisotropic morphology with high numbers of surface atoms and thus decrease the Pt utilization per mass (7–11). From the point of catalytic activity and durability, incorporating a second metal into the Pt lattice

to form bimetallic nanocrystals (NCs) is an effective way to modify the electron structure of Pt and thus tune the activity and durability of electrocatalysts. For example, Pt-Pd NCs with porous features are more active than Pt black catalysts for methanol oxidation reaction (12). Huang et al. (13) have demonstrated that doping the NCs with Mo can enhance the catalytic stability of electrocatalysts. Together, it is highly desirable to design multimetallic ultrathin Pt-based NW electrocatalysts with decreasing Pt utilization, superior activity, and durability.

To date, Pt-based NW electrocatalysts have been achieved through several approaches (14, 15). For example, Li et al. (16) demonstrated a galvanic replacement method for preparing Pt-Te alloy NWs using ultrathin Te NWs as both reducing agent and sacrificial template in ethylene glycol. Guo et al. (17) synthesized ultrathin Pt-Fe NWs with a diameter of ~2.5 nm and lengths ranging from 30 to 100 nm in a mixed solution of 1-octadecene, oleylamine (OAm), and sodium oleate. However, multimetallic Pt-based ultrathin NWs with an ultrahigh aspect ratio (a diameter of less than 3 nm and lengths of several micrometers) are difficult to synthesize and stabilize (18, 19). This is because, on the one hand, Pt atoms tend to form face-centered cubic (fcc) close-packed crystal structures during the crystal growth process; on the other hand, it is still difficult to control the reduction and nucleation process of multiple metal precursors at the same time due to their different reduction potentials. Here, we report an efficient $H_2$-assisted solution route (HASR) to synthesize ultrathin Pt-Mo-Ni NWs with a diameter of 2.5 nm and lengths of several micrometers. By combining the advantages of ultrathin 1D morphology, rich surface defects, and optimal metal compositions, the as-prepared Pt-Mo-Ni NWs exhibit better catalytic activity and durability toward ethanol electrooxidation than do commercial Pt black and Pt/C catalysts. Furthermore, we demonstrated that the HASR strategy can be extended to the preparation of other Pt-Mo-M (M = Fe, Co, Mn, Ru, etc.) NWs, paving the way for the design and synthesis of advanced ultrathin multimetallic electrocatalysts and for potential applications.

[1]Department of Chemistry, Tsinghua University, Beijing 100084, China. [2]Materials Characterization and Preparation Center, South University of Science and Technology of China, Shenzhen, Guangdong 518055, China. [3]Beijing Synchrotron Radiation Facility, Institute of High Energy Physics, Chinese Academy of Sciences, Beijing 100049, China. [4]Shanghai Synchrotron Radiation Facility, Shanghai Institute of Applied Physics, Chinese Academy of Sciences, Shanghai 201800, China. [5]Laboratory of Advanced Chemical Power Sources, Changchun Institute of Applied Chemistry, Chinese Academy of Sciences, Changchun, Jilin 130022, China. [6]Jilin Province Key Laboratory of Low Carbon Chemical Power Sources, Changchun, Jilin 130022, China. [7]State Key Laboratory of Advanced Technology for Materials Synthesis and Processing, Wuhan University of Technology, Wuhan 430070, China. [8]State Key Laboratory of Organic–Inorganic Composites and Beijing Advanced Innovation Center for Soft Matter Science and Engineering, Beijing University of Chemical Technology, Beijing 100029, China. [9]State Key Laboratory of Chemical Resource Engineering, Beijing University of Chemical Technology, Beijing 100029, China. [10]Department of Materials Science and Engineering, University of California, Los Angeles, Los Angeles, CA 90095, USA.
*These authors contributed equally to this work.
†Corresponding author. Email: wangdingsheng@mail.tsinghua.edu.cn (D.W.); ydli@mail.tsinghua.edu.cn (Y.L.)

## RESULTS AND DISCUSSION

Pt-Mo-Ni NWs were typically synthesized through thermal decomposition of $Mo(CO)_6$ and reduction of $Pt(acac)_2$ and $Ni(acac)_2$ under

$H_2$ atmosphere. The mixture was heated to 180°C and kept at this temperature for 10 hours (see Materials and Methods). The Pt-Mo-Ni NWs were obtained after washing and centrifugation. In this approach, $H_2$ serves as both reductant and structure-directing species, playing a key role in the formation of high-quality ultrathin Pt-Mo-Ni NWs. Figure 1 (A and B) shows the transmission electron microscopy (TEM) images of the as-obtained Pt-Mo-Ni NWs with different magnifications, which indicate that the products are composed of interconnected NWs with an ultrathin (~2.5 nm) and ultralong (several micrometers) nanostructure. Figure 1C shows the high-angle annular dark-field scanning TEM (HAADF-STEM) image of the Pt-Mo-Ni NWs. It is obvious that Pt-Mo-Ni NWs (inset in Fig. 1C) with a rough surface structure have a high density of low-coordinated atomic steps, ledges, and kinks (indicated by arrows) around the surface of the NWs. The aberration-corrected high-resolution HAADF-STEM image was used to investigate the obtained Pt-Mo-Ni NWs at the atomic scale. As shown in
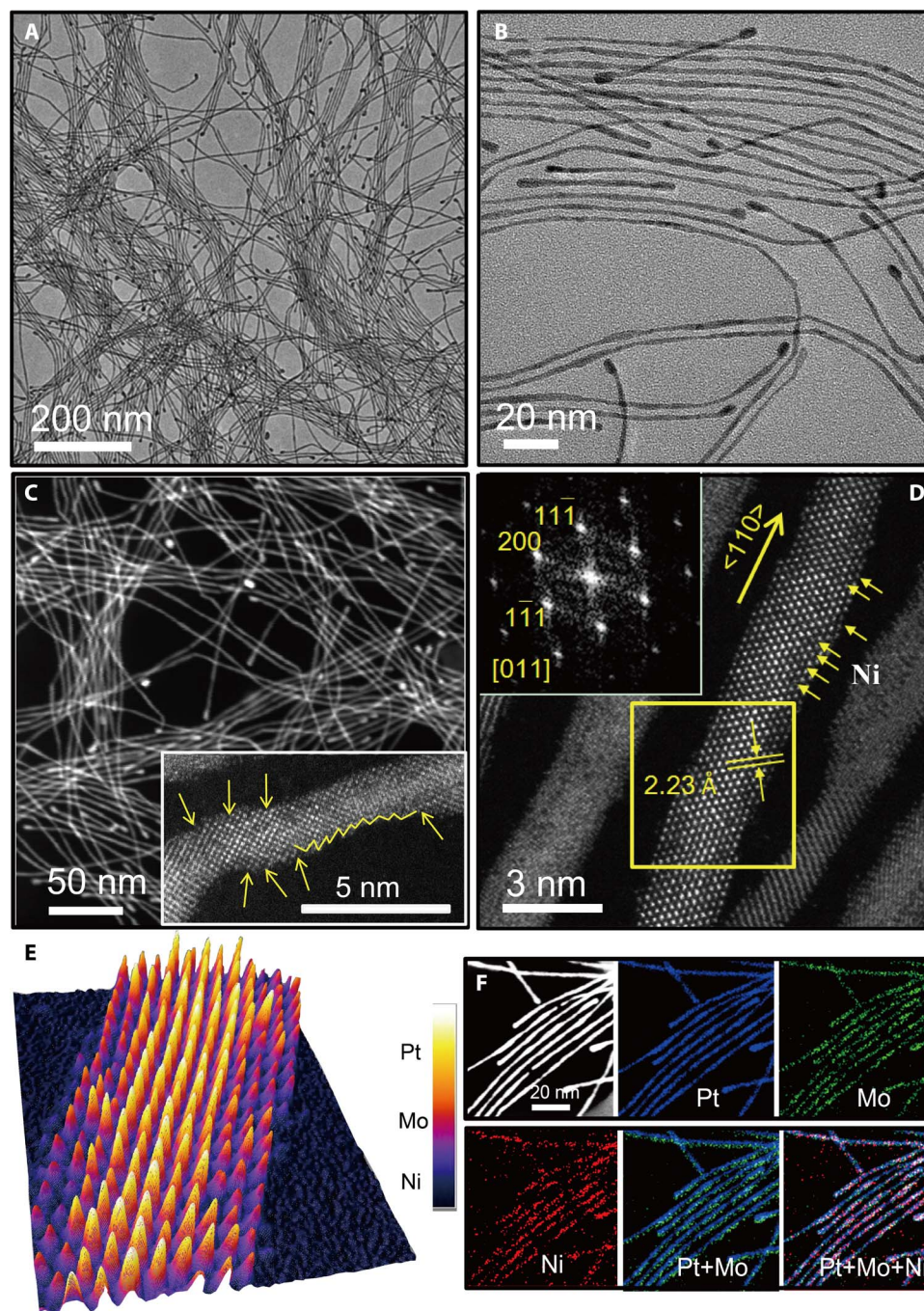


**Fig. 1. Structure characterization of the Pt-Mo-Ni NWs.** Low-magnification (**A**) and high-magnification (**B**) TEM images. (**C**) HAADF-STEM image. The yellow arrows indicate several atomic steps and corners. Inset: Enlarged image. (**D**) Atomic-resolution aberration-corrected HAADF-STEM image of Pt-Mo-Ni NWs. The yellow arrows show the Ni atoms, indicating that Pt was isolated by Ni atoms. Inset: FFT pattern. 3D HAADF-STEM intensity profile (**E**) and EDX mapping (**F**) of Pt-Mo-Ni NWs.

Fig. 1D and fig. S1, the continuous lattice fringes and selected-area fast Fourier transform (FFT) pattern reveal the single-crystalline nature of the Pt-Mo-Ni NWs, and the growth direction of the NW was along the <110> direction. The d-spacing for the adjacent lattice fringes measured was 0.22 nm, indicating the {111} facet of Pt-Mo-Ni NWs. Moreover, different brightness along the wires can be seen, where dark dots segregated at the edges of the NWs and bright dots appeared more centrally located. This observation indicates that the NWs with edges rich in Ni, Mo, and Pt on the surface were isolated by the Ni atoms (marked by arrows). Figure 1E shows the 3D HAADF-STEM intensity profiles, which exhibit uneven element distribution and defect-rich surface structure of Pt-Mo-Ni NWs. The unique element distribution of Pt-Mo-Ni NWs was further confirmed by energy-dispersive x-ray (EDX) elemental mapping (Fig. 1F). The discrete Ni image indicates that Ni atoms can isolate Pt atoms on the surface. We carried out a powder x-ray diffraction (XRD) experiment to identify the internal crystalline structure of the as-obtained products. As shown in fig. S2, the three distinct diffraction patterns could be indexed to the {111}, {200}, and {220} planes of the fcc structure. The XRD peak positions of the Pt-Mo-Ni NWs shifted to a higher angle compared to those of pure Pt, which could be attributed to the decreased lattice spacing that results from the replacement of Pt atoms by smaller Ni or Mo atoms. No detectable impurity peaks were detected in the XRD pattern, further indicating that only a single Pt-Mo-Ni phase exists in the product. The Pt/Mo/Ni atomic ratio determined by EDX analysis was 0.75:0.07:0.18 (fig. S3), which agreed with the result from inductively coupled plasma mass spectrometry (ICP-MS) analysis.

To understand the local atomic and electronic structures of the Pt-Mo-Ni NWs, we carried out ex situ x-ray absorption near-edge structure (XANES) and extended x-ray absorption fine structure (EXAFS) measurements. Figure 2A shows the normalized Pt $L_3$-edge XANES spectra of Pt-Mo-Ni NWs, with $PtO_2$ and Pt foil for reference. The oxidation state of Pt species can be monitored by white light intensity [20, 21], so the increased intensity of the Pt-Mo-Ni white line peak (at about 11572 eV, involving 2p–to–empty 5d transition) indicates that Pt in Pt-Mo-Ni is slightly oxidized compared with Pt foil. We can obtain additional information from the EXAFS spectra of the Pt $L_3$-edge, as shown in Fig. 2B. A small shoulder peak between 1.5 and 2.0 Å is found, which is derived from Pt-O coordination, also suggesting that Pt is mildly oxidized at the surface of the NWs, agreeing well with the XANES curves of Pt. The main peak located at 2.6 Å of the Pt $L_3$-edge spectra represents the nearest coordination shells of Pt atoms. The weaker intensity and shorter position of the main peak in Pt-Mo-Ni NWs indicate lesser first coordination number and shorter bond length than those of Pt foil due to alloying effects. The discrepancy of the oscillations in fig. S4A also indicates that the coordination environment of Pt in Pt-Mo-Ni NWs and Pt foil is quite different, because the phase of the EXAFS and the shape of the amplitude envelope provide information about the scatterer type [22]. The normalized Ni K-edge XANES spectra of Pt-Mo-Ni NWs, NiO bulk, and Ni foil are shown in Fig. 2C. Both the absorption edge position and white line peak intensity of Pt-Mo-Ni NWs are between that of NiO bulk and Ni foil. This indicates that the Ni oxidation state for Pt-Mo-Ni NWs is between $Ni^0$ and $Ni^{2+}$, which is consistent with the x-ray photoelectron spectroscopy results (fig. S11). Moreover, the Ni K-edge XANES spectra indicates that there may be two Ni species in the as-prepared Pt-Mo-Ni NWs: one in nickel oxide and one in Pt-Mo-Ni alloy [23]. The peak between 2.0 and 2.9 Å in the Ni K-edge FT-EXAFS spectra (Fig. 2D; the EXAFS oscillation functions are also given in fig. S4B) is quite obvious, and we cannot simply assign it to just one scattering path. Referring to the Ni K-edge FT spectra of NiO and

Ni foil, the peak at 2.0 to 2.9 Å may belong to the combination of two scattering paths: Ni-Ni scattering in NiO and Ni-Pt/Mo/Ni scattering in Pt-Mo-Ni alloy, similar to the result obtained from the XANES analysis of the Ni K-edge. Notably, there are also two Mo species in the Pt-Mo-Ni sample using the XANES and EXAFS discussion of the Mo K-edge (Fig. 2, E and F). The XANES feature of Pt-Mo-Ni is obviously different from Mo foil and $MoO_2$. The atomic structure of some Mo in the NWs is similar to that of $MoO_3$, with the appearance of the shoulder peak near the absorption edge for both Pt-Mo-Ni and $MoO_3$. The Mo K-edge position of Pt-Mo-Ni shifts to lower energy than does that of $MoO_2$ and $MoO_3$ because a part of Mo in the NWs is dispersed in the lattice of Pt and Ni, which is also demonstrated by EXAFS oscillation function and FT-EXAFS curve, as shown in fig. S4C and Fig. 2F, respectively [24, 25]. Additional information on the fitting results of the Pt $L_3$-edge, Ni K-edge, and Mo K-edge is provided in the Supplementary Materials (figs. S5 to S10 and tables S1 to S3).

Here, we report for the first time the synthesis of ultrathin Pt-Mo-Ni NWs using the HASR strategy. Previous research shows that $H_2$ has a positive impact on the formation of anisotropic and faceted particles [26, 27]. To examine whether $H_2$ was involved in the formation of Pt-Mo-Ni NWs, we performed the synthesis of Pt-Mo-Ni NWs under $H_2$-depleted conditions, in which an air atmosphere (fig. S12) or nitrogen-saturated (fig. S13) reaction solution was used and all other procedures were kept unchanged. Notably, we could not obtain ultrathin Pt-Mo-Ni NWs in the absence of $H_2$ and instead only yielded products with mixed morphologies (for example, nanoparticles, worm-like nanoparticles, and a small number of NWs), suggesting that the presence of $H_2$ may manipulate the growth kinetics of the reaction and thus tailor the size and morphology of the products. Moreover, when we accelerate the reaction rate by directly elevating the reaction temperature to 180°C, poor quality of NWs and a large amount of ultrasmall nanoparticles were obtained (fig. S14). The results further confirmed that the slow growth rate controlled by $H_2$ is critical to the formation of well-defined Pt-Mo-Ni NWs. To better understand the formation mechanism of the Pt-Mo-Ni NWs, we analyzed a series of samples collected at various stages of the reaction. When the reaction was performed at 50°C, the solution color became green and no products were obtained. With the elevation of the temperature from 50° to 120°C, the solution displayed gradual color evolution from green to dark green. This change suggests that the products started to form during the process. The ultrathin NWs were obtained at the bottom of the flask with a diameter of around 1 nm at 120°C (fig. S15). The molar ratio of Pt/Mo/Ni was determined to be 0.95:0.03:0.02. The red upper solution of the products collected at 120°C suggests that there are still amounts of Ni precursors present in the solution, as confirmed by ICP-MS. Furthermore, when the temperature was increased to 180°C, the solution turned black and a higher yield of NWs was achieved. TEM image shows that the morphology of NWs did not change (fig. S16), but the particle size increased with more Ni incorporation into Pt-rich NWs. The molar ratio of Pt/Mo/Ni collected at 180°C was 0.83:0.05:0.12, implying that the reduction of $Ni(acac)_2$ dominated the later growth process. When the reaction time was extended to 10 hours, well-defined Pt-Mo-Ni NWs were formed (fig. S17), and the molar ratio of Pt/Mo/Ni atoms was 0.75:0.07:0.18, which agreed with the final obtained composition. On the basis of the above results, a mechanism for the formation of Pt-Mo-Ni NWs can be summarized as follows (fig. S18): Beginning at 120°C, the Pt precursor is reduced to zero-value Pt atoms because of their high standard reduction potentials, and these Pt atoms will nucleate and grow to form Pt-rich NWs with the assistance of $H_2$. Here, $H_2$ serves as both the reduction
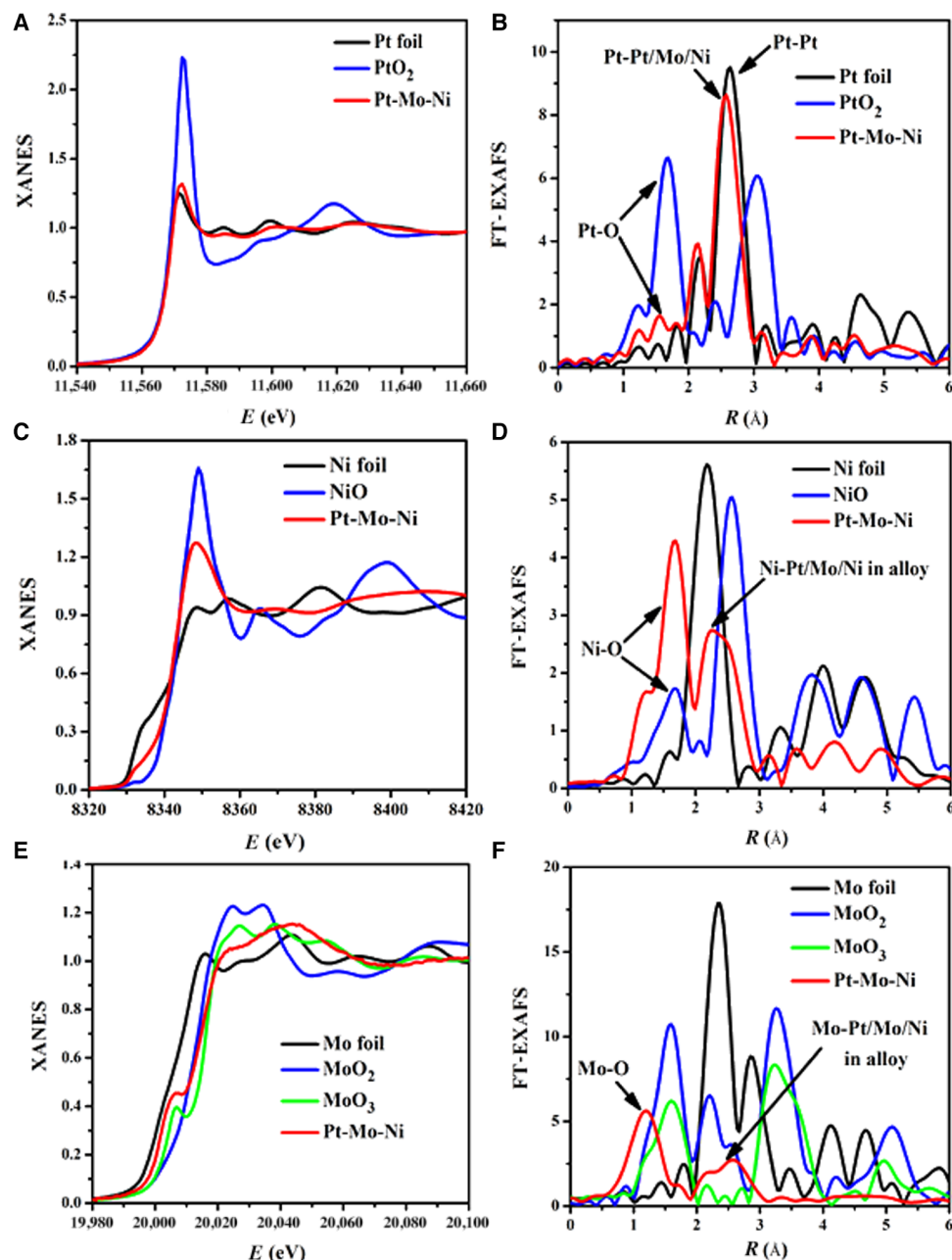
**Fig. 2. Structural analysis of the Pt-Mo-Ni NWs.** XANES (**A**) and EXAFS (**B**) analysis of Pt L$_3$-edge (FT range, 4.3 to 14.5 Å$^{-1}$). XANES (**C**) and EXAFS (**D**) analysis of Ni K-edge (FT range, 2.5 to 12.5 Å$^{-1}$). XANES (**E**) and EXAFS (**F**) analysis of Mo K-edge (FT range, 2.0 to 10.5 Å$^{-1}$).

and structure-directing species for controlling the reaction rate and further inducing the formation of NWs. The low packing density of OAm at the tip leads to the formation of NW, with two large nanoparticles on both ends. Upon increasing the reaction temperature (180°C), the zero-value Pt can further induce the stepwise reduction of Ni$^{2+}$ to Ni, and the formed Ni together with Mo atoms will then be adsorbed on the surface of Pt-rich NWs because the obtained intermediates have a higher surface energy. The subsequent growth does not change the overall NW morphology. After consumption of the metal precursors, the resultant stable phase of Pt-Mo-Ni is formed.

To elucidate the catalytic properties and potential applications of as-obtained ultrathin Pt-Mo-Ni NWs, we chose ethanol electrooxidation

to investigate the catalytic properties of Pt-Mo-Ni NWs. For comparison, commercial Pt/C and Pt black catalysts were selected and studied under the same condition. The typical cyclic voltammetric (CV) curves of the Pt black, commercial Pt/C, and Pt-Mo-Ni NWs in an argon-purged 0.5 M H$_2$SO$_4$ solution at a sweep rate of 50 mV/s are shown in fig. S19. All the catalysts exhibit distinct hydrogen adsorption/desorption processes present in the potential range of −0.2 to 0.1 V [versus saturated calomel electrode (SCE)] and Pt oxidation/reduction above 0.5 to 0.7 V (versus SCE). We compared the catalytic activity of these samples at the same potential (0.59 V versus SCE). The onset potential of Pt-Mo-Ni NWs was 100 mV, which is lower than that of commercial Pt/C (210 mV) and Pt black (220 mV) catalysts, indicating easier and faster

ethanol oxidation in the Pt-Mo-Ni NW catalysts. For specific activities (Fig. 3, A and B), the ethanol oxidation current density of Pt-Mo-Ni NWs (2.57 mA cm$^{-2}$) is 13.4 times that of the Pt/C catalyst (0.19 mA cm$^{-2}$) and 11.2 times that of the Pt black catalyst (0.23 mA cm$^{-2}$). With regard to mass activities, the current densities of Pt-Mo-Ni NWs (865.8 mA mg$^{-1}$) are 16.6 and 6.3 times those of Pt black (52.2 mA mg$^{-1}$) and Pt/C (137.5 mA mg$^{-1}$) catalysts. To further evaluate the stability of these catalysts, chronoamperometry (CA) curves (Fig. 3C) were recorded and compared. The as-prepared Pt-Mo-Ni NWs exhibited higher durability during the electrochemical measurements than did the commercial Pt black and Pt/C catalysts. In situ x-ray absorption spectroscopy (XAS) experiments were performed to investigate the structural stability of Pt-Mo-Ni NWs. The in situ XAFS of the Pt L$_3$-edge and Ni K-edge was carried out at the 1W1B station in the Beijing Synchrotron Radiation

Facility (BSRF) (a homemade electrochemical cell was used for in situ XAS measurements; all the data were recorded by a Lytle detector shown in fig. S20, A and B), and the in situ experiment of the Mo K-edge was performed at the 14W1 station in the Shanghai Synchrotron Radiation Facility (SSRF) (the spectra were collected using a solid-state detector shown in fig. S20, C and D). The XAFS curves of the Pt L$_3$-edge, Ni K-edge, and Mo K-edge were recorded at different voltages (0.0, 0.2, 0.4, and 0.6V). The atomic structure evolution of Pt, Ni, and Mo can be observed through the change of the FT-EXAFS curves (Fig. 3, D to F), as well as the XANES spectra (fig. S21, A, C, and E) and EXAFS oscillation functions (fig. S21, B, D, and F). The local atomic structure of Pt-Mo-Ni NWs was kept stable in the catalytic reaction process. The morphology and composition of Pt-Mo-Ni NWs were characterized after the reaction, which further confirmed the stable structure of the catalysts (for details,
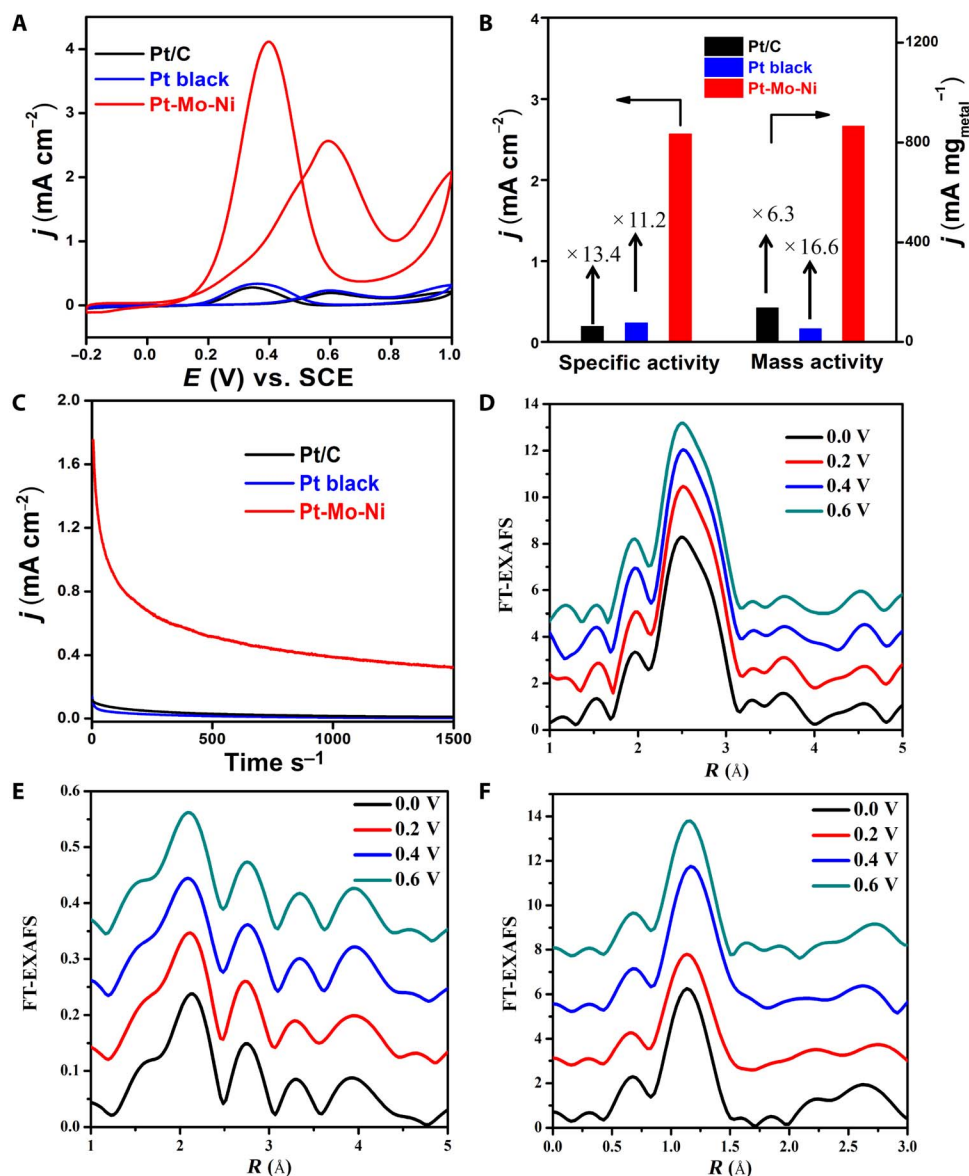


**Fig. 3. Electrochemical performance of the Pt-Mo-Ni NWs, Pt black, and Pt/C catalysts.** (**A**) Specific activities of Pt black and Pt/C catalysts and as-prepared Pt-Mo-Ni NWs recorded in 0.5 M H$_2$SO$_4$ + 2 M CH$_3$CH$_2$OH solution at a scan rate of 50 mV s$^{-1}$. (**B**) Graphical comparison of specific and mass activities of all catalysts. (**C**) CA results for these three catalysts. CA curves were recorded at 0.5 V versus SCE. FT-EXAFS curves of the Pt-Mo-Ni sample at different voltages. (**D**) Pt L$_3$-edge. (**E**) Ni K-edge. (**F**) Mo K-edge.

see figs. S22 to S24). To further verify the activities of Pt-Mo-Ni in the DEFC experiments, we also conducted a single-cell test. Figure S25 shows the corresponding steady-state polarization curves for Pt-Mo-Ni NWs and Pt/C catalysts. A higher maximum power density was obtained in the cell with Pt-Mo-Ni as the anode catalyst. Specifically, the maximum power density of Pt-Mo-Ni NWs at 60° and 80°C is 2.7 and 3.6 mW cm$^{-2}$, respectively, which is higher than that of the Pt/C catalyst.

The improvement of the catalytic activity and stability of the Pt-Mo-Ni NWs could be attributed to the following reasons. First, ultrathin Pt-Mo-Ni NWs with rich surface defects have high density of low-coordinated atoms, which not only decrease the Pt utilization per mass but also facilitate the oxidation of ethanol through a more effective way. Second, incorporation of 3d transition metals (Ni) into the Pt lattice to form ternary Pt-Mo-Ni NWs can promote the adsorption of hydroxyl species from water and then the removal of the poisoned CO intermediates at a lower potential compared to Pt/C and Pt black catalysts (28, 29). To further confirm this point, we conducted CO stripping (fig. S26) experiments. The peak potential of CO oxidation was in the order of Pt/C (0.64 V versus SCE) > Pt black (0.57 V versus SCE) > Pt-Mo-Ni (0.46 V versus SCE), indicating that the Pt-Mo-Ni catalysts have the priority in CO oxidation. Furthermore, the product testing results of this reaction indicated that the addition of a Ni element may probably favor the C–C bond activation and also the oxidation of adsorbates and/or intermediates to CO$_2$. Third, we carried out the density functional theory (DFT) calculations on the step edges of Pt-Mo-Ni NWs to elucidate the role of Mo and its stability in the Pt-Ni alloys (for details, see fig. S27 and table S4). The atomic cohesive energies, $E_{coh}$, of the Mo, whether at the surface (6.84 eV) or in the subsurface (8.61 or 8.42 eV), are larger than those of the Ni (5.58 eV) and Pt (5.67 eV). Both spatial confinement and energetic preference allow the Mo to be always retained in Pt-Ni NWs. Hence, the subsurface Mo atoms will increase the $E_{coh}$ of the Ni by 0.27 eV and of the Pt by 0.29 eV. This indicates that Mo has a stabilizing effect on undercoordinated sites of Pt-Ni NWs, which are the available sites for reactions. All these are attributed to the formation of relatively strong Mo–Pt and Mo–Ni bonds instead of Pt–Ni bonds. In this case, introducing Mo atoms in NWs fundamentally stabilizes both Ni and Pt atoms against dissolution and diffusion, which endow the catalyst with enhanced durability.

In addition to the ethanol electrooxidation of Pt-Mo-Ni NWs, we also applied the ultrathin Pt-Mo-Ni NWs as superior counter electrodes (CEs) for dye-sensitized solar cells (DSSCs). As shown in table S5, the Pt-Mo-Ni CEs have better efficiency than the Pt film CEs in DSSCs under AM1.5G (air mass 1.5 global) simulated solar light (100 mW cm$^{-2}$) (for more details, see figs. S28 to S31). The above result shows that trimetallic Pt-Mo-Ni NWs can act as potential multifunctional materials with high catalytic performance.

More importantly, the developed HASR strategy was also effective in the synthesis of other ultrathin ternary Pt-Mo-M (M = Fe, Co, Mn, Ru, etc.) NWs. Figure 4 (A, C, E, and G) shows typical STEM images of the as-prepared Pt-Mo-Fe, Pt-Mo-Co, Pt-Mo-Mn, and Pt-Mo-Ru NWs, respectively. It was clear that all the NWs exhibit ultrathin and ultralong characteristics and that part of them were spontaneously self-assembled into bundles. This is similar to what is seen in Pt-Mo-Ni NWs, indicating that the varied composition does not change the overall morphology of NWs. The unique structures and compositions of the prepared NWs are also visualized by EDX (figs. S32 to S35) and elemental mapping analysis (Fig. 4, B, D, F, and H). It can be observed that Pt, Mo, and M elements are distributed throughout the nanostructures, confirming the alloyed structure of the Pt-Mo-M NWs.

In conclusion, we successfully synthesized ultrathin Pt-Mo-Ni trimetallic NWs through a HASR strategy and demonstrated that H$_2$ is responsible for the well-controlled preparation of ultrathin trimetallic
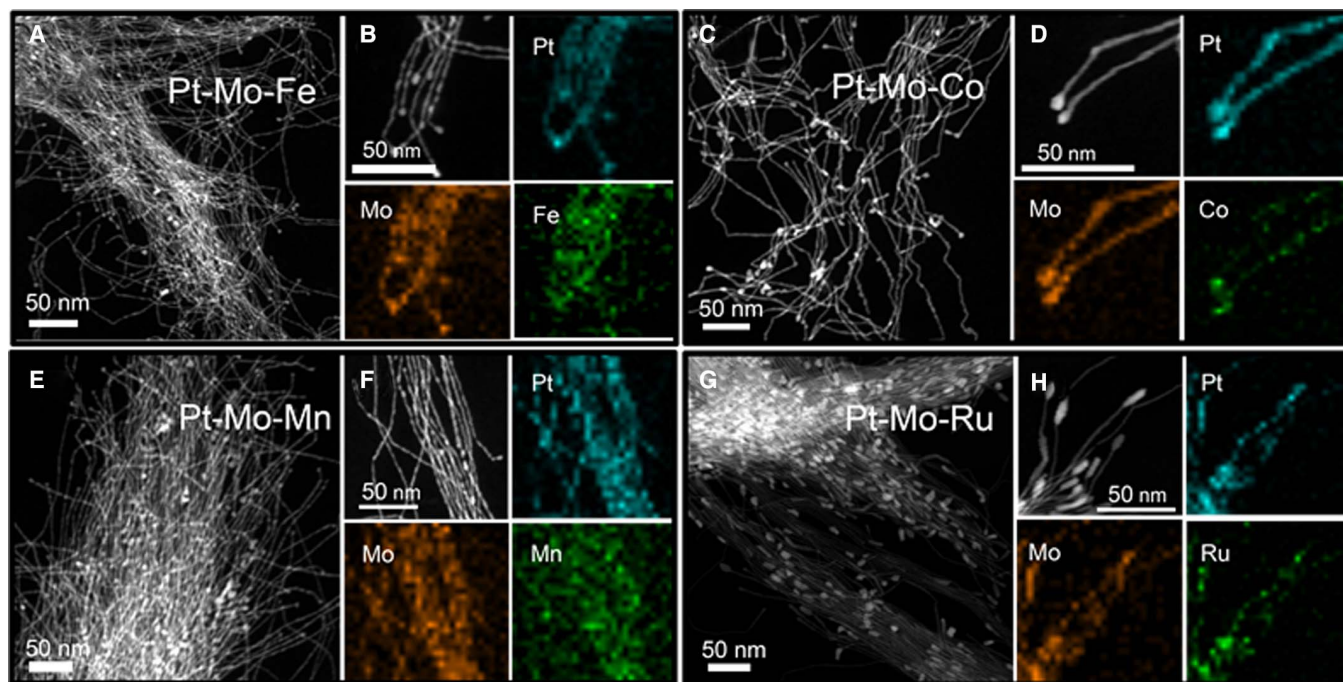
**Fig. 4. Synthesis of ultrathin ternary Pt-Mo-M (M = Fe, Co, Mn, Ru, etc.) NWs based on the HASR strategy.** HAADF-STEM image (**A**) and EDX mapping (**B**) of Pt-Mo-Fe NWs. HAADF-STEM image (**C**) and EDX mapping (**D**) of Pt-Mo-Co NWs. HAADF-STEM image (**E**) and EDX mapping (**F**) of Pt-Mo-Mn NWs. HAADF-STEM image (**G**) and EDX mapping (**H**) of Pt-Mo-Ru NWs.

NWs. Spherical aberration–corrected electron microscopy together with XAFS measurements confirmed the unique surface structure of as-prepared ultrathin NWs. Ni can isolate Pt atoms on the surface and produce surface defects, whereas Mo can stabilize these undercoordinated sites. Thus, the ultrathin Pt-Mo-Ni NWs showed high catalytic activity and substantially enhanced stability. Moreover, the developed HASR strategy can also be applied to synthesize a series of Pt-Mo-M (M = Fe, Co, Mn, Ru, etc.) NWs. We envision that this work will provide new insights into rational design and synthesis of cost-effective, active, and durable electrocatalysts.

## MATERIALS AND METHODS
### Preparation of Pt-Mo-Ni NWs
In a typical synthesis, 10.0 mg of Pt(acac)$_2$, 6.0 mg of Mo(CO)$_6$, 2.0 mg of Ni(acac)$_2$, and 10.0 mg of glucose were dissolved in 3.0 ml of OAm, followed by vigorous stirring for 30 min. The resulting homogeneous solution was transferred into a 10-ml Teflon-lined, high-pressure vessel. H$_2$ (30 bar) was introduced after the reactor was purged three times with H$_2$. The reaction vessel was then heated up to 180°C in an oil bath and maintained at this temperature for 10 hours before it was cooled to room temperature. The product was collected by centrifugation at 400 rpm for 2 min by using an ethanol-cyclohexane (volume ratio, 1:4) mixture. The ultrathin NWs were collected in the precipitate, then further washed several times with an ethanol-cyclohexane mixture, and finally dispersed in cyclohexane.

### Characterization
The powder XRD patterns were recorded with a Bruker D8 ADVANCE x-ray powder diffractometer with Cu Kα radiation (λ = 1.5406 Å). TEM and high-resolution TEM images were recorded by a JEOL JEM-1200EX working at 100 kV and an FEI Titan 80-300 transmission electron microscope equipped with a spherical aberration (Cs) corrector for the objective lens working at 300 kV. The composition of the product was measured by ICP-MS and EDX spectrometry.

### Electrochemical measurements
Electrochemical measurements were conducted on a computer-controlled electrochemical analyzer (CHI 660D) at room temperature. Catalyst-modified glassy carbon (GC) electrodes were used as working electrodes, Pt spiral wire was used as the CE, and saturated calomel electrode was used as the reference electrode. GC substrate electrodes were first polished with 0.3- and 0.05-μm Al$_2$O$_3$ slurry on a polishing cloth and then sonicated in ethanol and water each for several times. After the electrode was dried, a 5-μl suspension of the catalyst was dropped on a GC electrode. Aqueous solutions of 0.5 M H$_2$SO$_4$ containing 2 M ethanol were used for the electrolytes. All electrochemical experiments were performed at room temperature. The loading amount of Pt in the NW catalyst was 10.8 μg/cm$^2$. For comparison, the commercial Pt/C (size range of 3 to 4 nm) and Pt black catalysts, which have loading amounts of 8.2 and 20.4 μg/cm$^2$, respectively, were used as the benchmark catalyst. The electrochemically active surface area (ECSA) of the NW, Pt/C, and Pt black catalysts were calculated to be 33.7, 70.6, and 22.5 m$^2$/g, respectively.

### Ex situ XAFS measurements
The XAFS spectrum data (Pt L$_3$-edge, Ni K-edge, and Mo K-edge) were collected at the 1W1B station in BSRF (operated at 2.5 GeV with a maximum current of 250 mA) and the BL14W1 station in SSRF (operated at

3.5 GeV with a maximum current of 250 mA). The data were collected at room temperature (Pt L$_3$-edge in transmission mode using an N$_2$-filled ionization chamber, Ni K-edge in fluorescence excitation mode using a Lytle detector, and Mo K-edge in fluorescence excitation mode using a seven-element Ge detector). All samples were pelletized as discs (13 mm in diameter with a thickness of 1 mm) using graphite powder as a binder.

### In situ XAFS measurements
Electrochemical measurements were also conducted on a computer-controlled electrochemical analyzer. Catalyst-modified carbon paper was used as the working electrode, Pt spiral wire was used as the CE, and Ag/AgCl (KCl-saturated) electrode was used as the reference electrode. A homemade electrochemical cell was used for in situ XAS measurements. Details about the device are given in fig. S20.

The acquired EXAFS data were processed according to standard procedures using the ATHENA and ARTEMIS modules implemented in the IFEFFIT software package. The fitting detail is described below.

The acquired EXAFS data were processed according to standard procedures using the ATHENA module implemented in the IFEFFIT software package. The EXAFS spectra were obtained by subtracting the post-edge background from the overall absorption and then normalizing with respect to the edge-jump step. Subsequently, the $\chi(k)$ data were Fourier-transformed to real ($R$) space using Hanning windows ($dk = 1.0$ Å$^{-1}$) to separate the EXAFS contributions from different coordination shells. To obtain the quantitative structural parameters around the central atoms, least-squares curve parameter fitting was performed using the ARTEMIS module of the IFEFFIT software package (30).

The following EXAFS equation was used

$$\chi(k) = \sum_j \frac{N_j S_0^2 F_j(k)}{k R_j^2} \exp\left[-2k^2\sigma_j^2\right] \exp\left[\frac{-2R_j}{\lambda(k)}\right] \sin\left[2kR_j + \phi_j(k)\right]$$

where $S_0^2$ is the amplitude reduction factor, $F_j(k)$ is the effective curved-wave backscattering amplitude, $N_j$ is the number of neighbors in the $j$th atomic shell, $R_j$ is the distance between the x-ray absorbing central atom and the atoms in the $j$th atomic shell (backscatterer), $\lambda$ is the mean free path in angstrom, $\phi_j(k)$ is the phase shift (including the phase shift for each shell and the total central atom phase shift), and $\sigma_j$ is the Debye-Waller parameter of the $j$th atomic shell (variation of distances around the average $R_j$). The functions $F_j(k)$, $\lambda$, and $\phi_j(k)$ were calculated with the ab initio code FEFF8.2. Additional details for EXAFS simulations are given below.

The coordination numbers of model samples (Pt foil and PtO$_2$, Ni foil and NiO, and Mo foil and MoO$_3$) were fixed as the nominal values. The obtained $S_0^2$ was fixed in the subsequent fitting of the Pt L$_3$-edge, Ni K-edge, and Mo K-edge of Pt-Mo-Ni NWs, whereas the internal atomic distance $R$, Debye-Waller factor $\sigma^2$, and the edge-energy shift $\Delta E_0$ were allowed to run freely.

### Fuel cell test
A membrane electrode assembly (MEA), with 60 weight % (wt %) Pt/C (JM) or Pt-Mo-Ni/C as anode and 60 wt % Pt/C (Johnson Matthey, JM) as cathode, was prepared. The catalyst powder was mixed with isopropyl alcohol, deionized water, and 5 wt % Nafion solution (DuPont) to prepare the catalyst ink. Then, the well-mixed catalyst ink was sprayed onto the gas diffusion layer to fabricate the electrodes. The MEA was prepared by hot-pressing the anode and cathode electrodes

onto the two sides of the Nafion 115 membrane (DuPont) at 130°C for 2 min at 25 MPa. In MEAs, the amount of catalyst on the anode or cathode was 4.0 mg cm$^{-2}$. Considering the Pt loading in the catalyst, the amounts of Pt in Pt-Mo-Ni/C and Pt/C (JM) anode electrodes were 1.2 and 2.4 mg cm$^{-2}$, respectively. Single cells (25 cm$^2$) were assembled into a fuel cell fixture (qCf FC 25, balticFuelCells) for cell testing. Ethanol solution (1 M) was fed to the anode at a rate of 2.0 ml min$^{-1}$, and humidified oxygen gas was fed to the cathode at a rate of 200 ml min$^{-1}$. A fuel cell test system (Arbin Instruments) was used to obtain polarization and power density curves for the determination of real DEFC electrical performance under different temperatures. The polarization at 60° and 80°C was recorded to evaluate the catalytic ability.

## Methodology and calculation model

All spin-polarized DFT calculations were performed using VASP (Vienna Ab initio Simulation Package) (31). The generalized gradient approximation of PW91 (32) and the projector augmented-wave method (33, 34) were used to describe the exchange-correlation functional and the electron-ion interaction, respectively. A cutoff energy of 340 eV was used. According to the characterization results from Fig. 1 (C and D), the stepped Pt (221) surface was taken as a representative of the lateral faces of ultrathin NWs. In the model approximation, the main structural characteristics of Pt NWs [the {110} step edge in Pt (221) that is of {111} structures] were maintained. In this way, the stepped Pt (221) could allow for the anisotropic growth of NWs, different from NCs (13). In practice, a six-layer Pt (221) slab with a (1 × 3) unit cell was used to model the step edge of Pt NWs (fig. S27A). The vacuum spacing between slabs was 12 Å. A Monkhorst-Pack k-point mesh of 4 × 4 × 1 was applied to sample the first Brillouin zones of surface. The top three layers were relaxed, whereas the other three layers were fixed at their bulk-truncated structure. The convergence criterion of optimization was set to 0.03 eV Å$^{-1}$ for the energy gradient. Bader charge analysis was used to calculate the charge transfer (35).

$E_{coh}$ was defined as the energy needed to remove a metal atom (M) from the alloy NWs

$$E_{coh} = E_{N-1} + E_M - E_N$$

where $E_{N-1}$ and $E_N$ are the total energies of systems with the numbers of N−1 and N atoms, and $E_M$ is the energy of the M atom removed. From the energetic point of view, the atomic cohesive energy to a certain extent reflected the stability of the metal atoms in systems (36). Here, we focused on the doping effects of the Mo at the surface and subsurface of {110} step edges. The surface defects with undercoordinated sites are more active than the {111} facets and are always the available sites for reactions (37). The schematics of Mo-doped Pt-Ni {110} step edges in (221) are illustrated in fig. S27B.

## SUPPLEMENTARY MATERIALS

Supplementary material for this article is available at http://advances.sciencemag.org/cgi/content/full/3/8/e1603068/DC1

## REFERENCES AND NOTES

1. C. Lamy, T. Jaubert, S. Baranton, C. Coutanceau, Clean hydrogen generation through the electrocatalytic oxidation of ethanol in a Proton Exchange Membrane Electrolysis Cell (PEMEC): Effect of the nature and structure of the catalytic anode. J. Power Sources 245, 927–936 (2014).
2. Y. Bing, H. Liu, L. Zhang, D. Ghosh, J. Zhang, Nanostructured Pt-alloy electrocatalysts for PEM fuel cell oxygen reduction reaction. Chem. Soc. Rev. 39, 2184–2202 (2010).
3. B. Y. Xia, H. B. Wu, N. Li, Y. Yan, X. W. Lou, X. Wang, One-pot synthesis of Pt-Co alloy nanowire assemblies with tunable composition and enhanced electrocatalytic properties. Angew. Chem. 127, 3868–3872 (2015).
4. F. Nosheen, Z. Zhang, G. Xiang, B. Xu, Y. Yang, F. Saleem, X. Xu, J. Zhang, X. Wang, Three-dimensional hierarchical Pt-Cu superstructures. Nano Res. 8, 832–838 (2015).
5. Y. Tan, J. Fan, G. Chen, N. Zheng, Q. Xie, Au/Pt and Au/Pt$_3$Ni nanowires as self-supported electrocatalysts with high activity and durability for oxygen reduction. Chem. Commun. 47, 11624–11626 (2011).
6. Z. Niu, N. Becknell, Y. Yu, D. Kim, C. Chen, N. Kornienko, G. Somorjai, P. Yang, Anisotropic phase segregation and migration of Pt in nanocrystals en route to nanoframe catalysts. Nat. Mater. 15, 1188–1194 (2016).
7. L. Bu, J. Ding, S. Guo, X. Zhang, D. Su, J. Yao, J. Guo, G. Lu, X. Huang, A general method for multimetallic platinum alloy nanowires as highly active and stable oxygen reduction catalysts. Adv. Mater. 27, 7204–7212 (2015).
8. L. Bu, S. Guo, X. Zhang, X. Shen, D. Su, G. Lu, X. Zhu, J. Yao, J. Guo, X. Huang, Surface engineering of hierarchical platinum-cobalt nanowires for efficient electrocatalysis. Nat. Commun. 7, 11850–11859 (2016).
9. L. Zhang, N. Li, F. Gao, L. Hou, Z. Xu, Insulin amyloid fibrils: An excellent platform for controlled synthesis of ultrathin superlong platinum nanowires with high electrocatalytic activity. J. Am. Chem. Soc. 134, 11326–11329 (2012).
10. L. Ruan, E. Zhu, Y. Chen, Z. Lin, X. Huang, X. Duan, Y. Huang, Biomimetic synthesis of an ultrathin platinum nanowire network with a high twin density for enhanced electrocatalytic activity and durability. Angew. Chem. Int. Ed. 52, 12577–12581 (2013).

11. H.-W. Liang, X. Cao, F. Zhou, C.-H. Cui, W.-J. Zhang, S.-H. Yu, A free-standing Pt-nanowire membrane as a highly stable electrocatalyst for the oxygen reduction reaction. *Adv. Mater.* **23**, 1467–1471 (2011).

12. L. Wang, Y. Yamauchi, Metallic nanocages: Synthesis of bimetallic Pt–Pd hollow nanoparticles with dendritic shells by selective chemical etching. *J. Am. Chem. Soc.* **135**, 16762–16765 (2013).

13. X. Huang, Z. Zhao, L. Cao, Y. Chen, E. Zhu, Z. Lin, M. Li, A. Yan, A. Zettl, Y. Wang, X. Duan, T. Mueller, Y. Huang, High-performance transition metal–doped $Pt_3Ni$ octahedra for oxygen reduction reaction. *Science* **348**, 1230–1234 (2015).

14. Q. Xiao, M. Cai, M. P. Balogh, M. M. Tessema, Y. Lu, Symmetric growth of Pt ultrathin nanowires from dumbbell nuclei for use as oxygen reduction catalysts. *Nano Res.* **5**, 145–151 (2012).

15. J.-I. Shui, C. Chen, J. C. M. Li, Evolution of nanoporous Pt-Fe alloy nanowires by dealloying and their catalytic property for oxygen reduction reaction. *Adv. Funct. Mater.* **21**, 3357–3362 (2011).

16. H.-H. Li, S. Zhao, M. Gong, C.-H. Cui, D. He, H.-W. Liang, L. Wu, S.-H. Yu, Ultrathin PtPdTe nanowires as superior catalysts for methanol electrooxidation. *Angew. Chem. Int. Ed.* **52**, 7472–7476 (2013).

17. S. Guo, D. Li, H. Zhu, S. Zhang, N. M. Markovic, V. R. Stamenkovic, S. Sun, FePt and CoPt nanowires as efficient catalysts for the oxygen reduction reaction. *Angew. Chem. Int. Ed.* **125**, 3549–3553 (2013).

18. G. Fu, X. Yan, Z. Cui, D. Sun, L. Xu, Y. Tang, J. Goodenough, J.-M. Lee, Catalytic activities for methanol oxidation on ultrathin $CuPt_3$ wavy nanowires with/without smart polymer. *Chem. Sci.* **7**, 5414–5420 (2016).

19. M. E. Scofield, C. Koenigsmann, L. Wang, H. Liu, S. Wong, Tailoring the composition of ultrathin, ternary alloy PtRuFe nanowires for the methanol oxidation reaction and formic acid oxidation reaction. *Energy Environ. Sci.* **8**, 350–363 (2015).

20. F. W. Lytle, P. S. P. Wei, R. B. Greegor, G. H. Via, J. H. Sinfelt, Effect of chemical environment on magnitude of x-ray absorption resonance at $L_{III}$ edges. Studies on metallic elements, compounds, and catalysts. *J. Chem. Phys.* **70**, 4849–4855 (1979).

21. J. A. Horsley, Relationship between the area of $L_{2,3}$ x-ray absorption edge resonances and the *d* orbital occupancy in compounds of platinum and iridium. *J. Chem. Phys.* **76**, 1451–1458 (1982).

22. J. E. Penner-Hahn, X-ray absorption spectroscopy in coordination chemistry. *Coord. Chem. Rev.* **190–192**, 1101–1123 (1999).

23. N. Becknell, Y. Kang, C. Chen, J. Resasco, N. Kornienko, J. Guo, N. Markovic, G. Somorjai, V. Stamenkovic, P. Yang, Atomic structure of $Pt_3Ni$ nanoframe electrocatalysts by in situ X-ray absorption spectroscopy. *J. Am. Chem. Soc.* **137**, 15817–15824 (2015).

24. J. Ge, D. He, W. Chen, H. Ju, H. Zhang, T. Chao, X. Wang, R. You, Y. Lin, Y. Wang, J. Zhu, H. Li, B. Xiao, W. Huang, Y. Wu, X. Hong, Y. Li, Atomically dispersed Ru on ultrathin Pd nanoribbons. *J. Am. Chem. Soc.* **138**, 13850–13853 (2016).

25. R. Long, Y. Li, Y. Liu, S. Chen, X. Zheng, C. Gao, C. He, N. Chen, Z. Qi, L. Song, J. Jiang, J. Zhu, Y. Xiong, Isolation of Cu atoms in Pd lattice: Forming highly selective sites for photocatalytic conversion of $CO_2$ to $CH_4$. *J. Am. Chem. Soc.* **139**, 4486–4492 (2017).

26. J. Ren, R. Tilley, Shape-controlled growth of platinum nanoparticles. *Small* **3**, 1508–1512 (2007).

27. Y. Kang, X. Ye, C. B. Murray, Size- and shape-selective synthesis of metal nanocrystals and nanowires using CO as a reducing agent. *Angew. Chem. Int. Ed.* **49**, 6156–6159 (2010).

28. J. Mathiyarasu, A. M. Remona, A. Mani, K. L. N. Phani, V. Yegnaraman, Exploration of electrodeposited platinum alloy catalysts for methanol electro-oxidation in 0.5 M $H_2SO_4$: Pt-Ni system. *J. Solid State Electrochem.* **8**, 968–975 (2004).

29. R. Mu, Q. Fu, H. Xu, H. Zhang, Y. Huang, Z. Jiang, S. Zhang, D. Tan, X. Bao, Synergetic effect of surface and subsurface Ni species at Pt–Ni bimetallic catalysts for CO oxidation. *J. Am. Chem. Soc.* **133**, 1978–1986 (2011).

30. B. Ravel, M. Newville, *ATHENA, ARTEMIS, HEPHAESTUS*: Data analysis for X-ray absorption spectroscopy using *IFEFFIT*. *J. Synchrotron. Radiat.* **12**, 537–541 (2005).

31. G. Kresse, J. Furthmüller, Efficient iterative schemes for *ab initio* total-energy calculations using a plane-wave basis set. *Phys. Rev. B Condens. Matter* **54**, 11169–11186 (1996).

32. J. P. Perdew, Y. Wang, Accurate and simple analytic representation of the electron-gas correlation energy. *Phys. Rev. B* **45**, 13244–13249 (1992).

33. P. E. Blöchl, Projector augmented-wave method. *Phys. Rev. B* **50**, 17953–17979 (1994).

34. G. Kresse, D. Joubert, From ultrasoft pseudopotentials to the projector augmented-wave method. *Phys. Rev. B* **59**, 1758–1775 (1999).

35. G. Henkelman, A. Arnaldsson, H. Jónsson, A fast and robust algorithm for Bader decomposition of charge density. *Comput. Mater. Sci.* **36**, 354–360 (2006).

36. C. D. Taylor, M. Neurock, J. R. Scully, First-principles investigation of the fundamental corrosion properties of a model Cu nanoparticle and the (111), (113) surfaces. *J. Electrochem. Soc.* **155**, C407–C414 (2008).

37. Y. Wu, D. Wang, X. Chen, G. Zhou, R. Yu, Y. Li, Defect-dominated shape recovery of nanocrystals: A new strategy for trimetallic catalysts. *J. Am. Chem. Soc.* **135**, 12220–12223 (2013).

**Citation:** J. Mao, W. Chen, D. He, J. Wan, J. Pei, J. Dong, Y. Wang, P. An, Z. Jin, W. Xing, H. Tang, Z. Zhuang, X. Liang, Y. Huang, G. Zhou, L. Wang, D. Wang, Y. Li, Design of ultrathin Pt-Mo-Ni nanowire catalysts for ethanol electrooxidation. *Sci. Adv.* **3**, e1603068 (2017).